Pedro Américo A. M. Júnior
pamerico@pucminas.br
Pontifícia Universidade Católica de Minas Gerais
Departamento de Engenharia Mecânica
Av. Dom Jose Gaspar, 500, Coração Eucarístico
30535-901 Belo Horizonte, MG, Brasil

Cristina Almeida Magalhães
crisamagalhaes@hotmail.com
Centro Universitário Newton Paiva
Coordenações das Engenharias
Rua José Cláudio Rezende, 420, Estoril
30455-590 Belo Horizonte, MG, Brasil

Perrin Smith Neto
psmith@pucminas.br
Pontifícia Universidade Católica de Minas Gerais
Departamento de Engenharia Mecânica
Av. Dom Jose Gaspar, 500, Coração Eucarístico
30535-901 Belo Horizonte, MG, Brasil

New Numerical Method for the Photoelastic Technique

The objective of this research is to find new equations for a novel phase-shifting method in digital photoelasticity. Some innovations are proposed. In terms of phase-shifting, only the analyzer is rotated, and the other equations are deduced by applying a new numerical technique instead of the usual algebraic techniques. This approach can be used to calculate a larger sequence of images. Each image represents a measurement of the stresses present in the object. Every photographic image has errors and random noise, but the uncertainties due to these effects can be reduced with a larger number of observations.
Keywords: *photoelasticity, metrology, stress analysis, optical measurement*

Introduction

Photoelasticity is one of the oldest methods for experimental stress analysis, but it has been overshadowed by the Finite Element Method for engineering applications over the past two to three decades. However, certain new and novel developments and applications have revived the use of photoelasticity. The new approach involves the use of hybrid methods in which the advantages of both experimental and numerical methods are exploited. Nevertheless, recent industrial needs, such as the continuous on-line monitoring of structures, determination of the residual stresses in glass (plastics) and microelectronics materials, rapid prototype production and dynamic visualization of stress waves, have brought photoelasticity into the limelight once again (Asundi, 2001).

The current trend of digitally imaging photoelastic fringe patterns indicates that image processing can be used to delineate the required information from the fringe patterns. The phase-shifting method has the most potential, particularly with respect to fringe sign determination. The method of photoelasticity makes it possible to obtain the principal stress directions and principal stress differences in a model. The principal stress directions and the principal stress differences are provided by isoclinics and isochromatics, respectively (Asundi, Tong and Boay, 2001). Isoclinics are the loci of the points in the specimen along which the principal stresses lie in the same direction. Isochromatics are the loci of the points along which the difference in the first and second principal stress remains the same. Thus, they are the lines that join the points with equal maximum shear stress magnitudes (Fernandez, 2011).

The fringe patterns are nothing but the record of the phase difference between light travelling in two different optical paths as intensity variations. By varying the phase difference between the beams involved, in known steps, it is possible to generate a sufficient number of equations to solve the parameters involved. In general, phase differences can be added by altering the optical path length of any one of the light beams. Usually, the phase of the reference light beam is altered in known steps. Photoelasticity falls into a special category, in that the two light beams cannot be treated separately, but rather always go together (Kihara, 2007). This means a phase shift introduced in one light beam will also introduce a corresponding phase shift in the other beam. This change in phase, in practice, is achieved by appropriately rotating the optical elements of the polariscope. A detailed study of the intensity of the light transmitted can help in relating the rotation of the optical elements to the change in phase introduced (Huang and Sung, 2010).

Nomenclature

$b_{r,s}$ = *coefficients of the numerator in the new equations for calculating phase α, dimensionless*
$c_{r,s}$ = *coefficients of the denominator in the new equations for calculating phase α, dimensionless*
D = *diameter of the disk, m*
E_x,E_y = *the components of electric field in light along and perpendicular to the analyzer axis, N/C*
E_a,E_δ = *average error, difference between values measured in the experiments and the values calculated by the theory of elasticity, rad*
$e_{r,s}$ = *coefficients of the numerator in the new equations for calculating phase δ, dimensionless*
F = *material fringe constant photoelastic, N/m*
$f_{r,s}$ = *coefficients of the denominator in the new equations for calculating phase δ, dimensionless*
H = *thickness of the disk, m*
K = *constant proportion of the maximum light intensity emerging from the analyzer, dimensionless*
k = *amplitude of light vector, N/C*
I = *the output light intensity in the photographic image, dimensionless*
M = *number of pixels of the image, dimensionless*
N = *number of images, dimensionless*
n = *isochromatic fringe orders, dimensionless*
P = *diametrical compress load, N*
r = *integer counter, dimensionless*
$Step$ = *integer values greater than or equal to 3, dimensionless*
s = *integer counter, dimensionless*
x = *horizontal distance from the origin at the center of disk, m*
y = *vertical distance from the origin at the center of disk, m*

Paper received 8 March 2012. Paper accepted 22 July 2012
Technical Editor: Lavinia Borges

Greek Symbols

$\Delta\theta$ = *increase given the angle of the analyzer in each photographic image, rad*
α = *angle between the direction and the axis of σ_1 horizontal reference, rad*
δ = *delay in the model given by the photoelastic isochromatic fringes, rad*
φ = *angle of the second quarter-wave plate in polariscope relative to the horizontal axis x, rad*
π = *mathematical constant that is the ratio of a circle's circumference to its diameter, (3.14159265358979323846264 3), dimensionless*
θ = *angle of the analyzer in polariscope relative to the horizontal axis x, rad*
σ_x, σ_y = *Cartesian components of normal stresses, Pa*
σ_1, σ_2 = *principal normal stresses, Pa*
τ_{xy} = *Cartesian shear stress component, Pa*
ω = *angular frequency of light vector, rad*

Subscripts

e = *indicates the exact, analytical values*
r = *relative to the line counter index*
s = *relative to the column index counter*
x = *relative to the horizontal axis (Cartesian)*
y = *relative to the vertical axis (Cartesian)*
v = *relative to the number of restrictions in the new mathematical model of linear programming*

Phase-Shifting Methods of Analysis

The optical arrangement to recognize and to identify isoclinics and isochromatics from photoelastic fringes is a circular polariscope set-up, shown in Fig. 1. In Fig. 1, *P*, *Q*, *R*, and *A* represent the polarizer, quarter-wave plate, retarder (stressed model) and analyzer, respectively. The orientation of the element is written by a subscript, which means the angle between the polarizing axis and the horizontal *x* axis. $R_{\alpha\delta}$ represents the stressed sample taken as a retardation δ and whose fast axis is at an angle α with the *x* axis (Baek et al., 2002). Therefore, $P_{90}Q_{45}R_{\alpha\delta}\ Q_{-45}A_{\theta}$ indicates the following: a polarizer at 90°, a quarter-wave plate with a fast axis at 45°, a specimen as retardation δ whose fast axis is at an angle α with the *x* axis, a quarter-wave plate with a fast axis at –45°, and an analyzer at θ. With the Jones calculus (Collect, 2005) for the arrangement of $P_{90}Q_{45}R_{\alpha\delta}Q_{-45}A_{\theta}$ shown in Fig. 1, the components of the electric field in light along and perpendicular to the analyzer axis (E_x, E_y) are given as

$$\begin{pmatrix} E_x \\ E_y \end{pmatrix} = \begin{bmatrix} \cos^2\theta & \sin\theta\cos\theta \\ \sin\theta\cos\theta & \sin^2\theta \end{bmatrix} \times \begin{bmatrix} 1+i & 1-i \\ 1-i & 1+i \end{bmatrix} \times \begin{bmatrix} e^{i\delta}\cos^2\alpha + \sin^2\alpha & \left(e^{i\delta}-1\right)\sin\alpha\cos\alpha \\ \left(e^{i\delta}-1\right)\sin\alpha\cos\alpha & e^{i\delta}\cos^2\alpha + \sin^2\alpha \end{bmatrix} \times \left(\frac{i+1}{4}\right) \begin{bmatrix} 1 & i \\ i & 1 \end{bmatrix} \begin{pmatrix} 0 \\ 1 \end{pmatrix} ke^{iwt} \quad (1)$$

where $i = \sqrt{-1}$, θ and $\varphi = -45°$ are the angles that the analyzer and the second quarter-wave plate form with the reference *x* axis, respectively. The symbols *k* and ω are the amplitude and the angular frequency of the light vector, respectively.

$$I = \overline{E_x}E_y + \overline{E_y}E_x \quad (2)$$

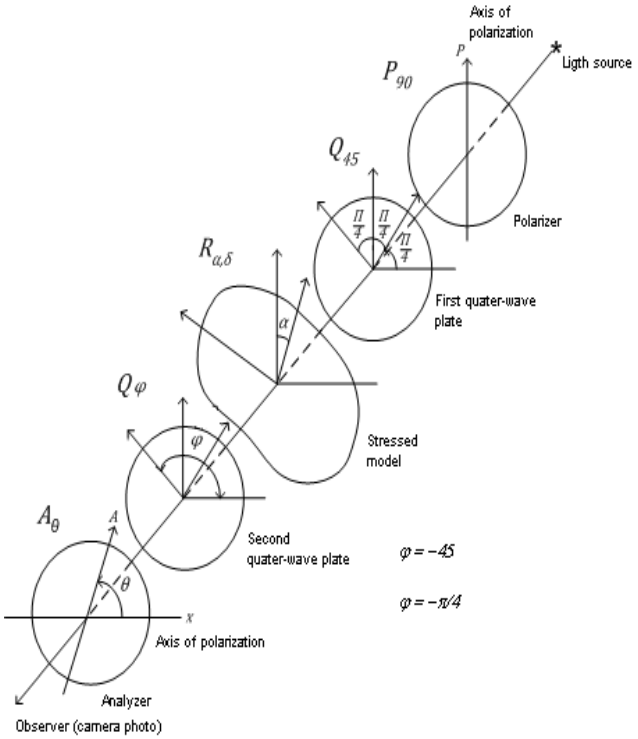

Figure 1. Optical arrangement of a circular polariscope (180º = π radians).

In Eq. (2), *I* is the output light intensity, and $\overline{E_x}$ and $\overline{E_y}$ are the complex conjugate of E_x and E_y, respectively. After the simple operation of Eq. (1) by Eq. (2), the output intensity of the circular polariscope for the arrangement $P_{90}Q_{45}R_{\alpha\delta}Q_{-45}A_{\theta}$ is given by

$$I = K\left[1 - \cos(2\theta)\cos(\delta) - \cos(2\alpha)\sin(2\theta)\sin(\delta)\right] \quad (3)$$

where *K* is a proportional constant, i.e., the maximum light intensity emerging from the analyzer. These angle values are chosen to simplify the calibration of the polariscope used in the experiments measurements. For the phase measuring technique, the angle α and the relative retardation δ indicating the direction and the difference of principal stresses, respectively, are the parameters to be obtained.

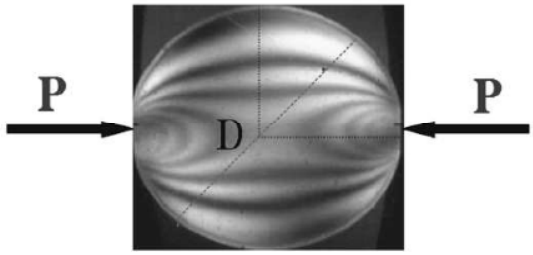

Figure 2. Sample under compression.

In the experiments, Fig. 2, the diameter and the thickness of the disk used are *D* = 10.0 cm and *H* = 0.5 cm, respectively. A diametrical compression load, *P* = 50.0 N, is applied to the disk. The material fringe constant *F* = 5.2500 N/cm is used. From the given conditions, the theoretical value of isochromatic δ is related to two principal stress components, σ_1 and σ_2, as in Eq. (4). In contrast, the

theoretical isocline angle α can be calculated by Eq. (5) using stress components σ_x, σ_y, and τ_{xy}.

$$\delta = \frac{2\pi H}{F}(\sigma_1 - \sigma_2) \tag{4}$$

$$\alpha = \frac{1}{2}\tan^{-1}\left(\frac{2\tau_{xy}}{\sigma_x - \sigma_y}\right) \tag{5}$$

In the literature on the theory of elasticity (Ng, 1997; Oh and Kim, 2003), the exact value of the stress field, for a function of x and y with its origin at the center of the disc is given by (the superscript "e" indicates the exact, analytical values):

$$\sigma_x^e = \frac{-2P}{\pi H}\left\{\frac{(D/2-y)x^2}{\left[x^2+(D/2-y)^2\right]^2} + \frac{(D/2+y)x^2}{\left[x^2+(D/2+y)^2\right]^2} - \frac{1}{D}\right\} \tag{6}$$

$$\sigma_y^e = \frac{-2P}{\pi H}\left\{\frac{(D/2-y)^3}{\left[x^2+(D/2-y)^2\right]^2} + \frac{(D/2+y)^3}{\left[x^2+(D/2+y)^2\right]^2} - \frac{1}{D}\right\} \tag{7}$$

$$\tau_{xy}^e = \frac{2P}{\pi H}\left\{\frac{(D/2-y)^2 x}{\left[x^2+(D/2-y)^2\right]^2} + \frac{(D/2+y)^2 x}{\left[x^2+(D/2+y)^2\right]^2}\right\} \tag{8}$$

For comparison with the experimentally measured values, the following are used:

$$\sigma_1^e = \frac{\left(\sigma_x^e + \sigma_y^e\right)}{2} - \sqrt{\frac{1}{4}\left(\sigma_x^e - \sigma_y^e\right)^2 + \left(\tau_{xy}^e\right)^2} \tag{9}$$

$$\sigma_2^e = \frac{\left(\sigma_x^e + \sigma_y^e\right)}{2} + \sqrt{\frac{1}{4}\left(\sigma_x^e - \sigma_y^e\right)^2 + \left(\tau_{xy}^e\right)^2} \tag{10}$$

Then, with Eq. (11) and Eq. (12), the exact values of δ^e and α^e can be calculated for each point of the x and y coordinates in the same manner as in Eq. (4) and Eq. (5):

$$\delta^e = \frac{2\pi H}{F}(\sigma_1^e - \sigma_2^e) \tag{11}$$

$$\alpha^e = \frac{1}{2}\tan^{-1}\left(\frac{2\tau_{xy}^e}{\sigma_x^e - \sigma_y^e}\right) \tag{12}$$

Figures 3 and 4 show the result of applying the analytical equations 11 and 12, the color change over a range of $\pi/4$ radians in order to simulate the formation of fringes. The idea is to compare these exact results (δ^e and α^e) obtained theoretically in the analysis of stress with experimental measurements of light intensities using the proposed method (δ and α).

New Mathematical Model

By analogy to the equations of phase calculation used by other authors and the mathematical model proposed in Magalhaes, Neto and Barcellos (2010), we had the idea to try a new general model for the equations of phase in photoelasticity. After many different attempts, a general equation for calculating the phase for any number, N, of images is proposed:

$$\alpha = \frac{1}{2}\tan^{-1}\left(\frac{\sqrt{\left|\sum_{r=1}^{N}\sum_{s=r}^{N} b_{r,s} I_r I_s\right|}}{\sqrt{\left|\sum_{r=1}^{N}\sum_{s=r}^{N} c_{r,s} I_r I_s\right|}}\right) \tag{13}$$

$$\delta = \tan^{-1}\left(\frac{\sqrt{\left|\sum_{r=1}^{N}\sum_{s=r}^{N} e_{r,s} I_r I_s\right|}}{\sqrt{\left|\sum_{r=1}^{N}\sum_{s=r}^{N} f_{r,s} I_r I_s\right|}}\right) \tag{14}$$

where N is the number of images, $b_{r,s}$ and $e_{r,s}$ are coefficients of the numerator, $c_{r,s}$ and $f_{r,s}$ are coefficients of the denominator, and r and s are the index of the sum (Magalhaes, Neto and Barcellos, 2010). Expanding the summations and allowing an arbitrary number of lines yields

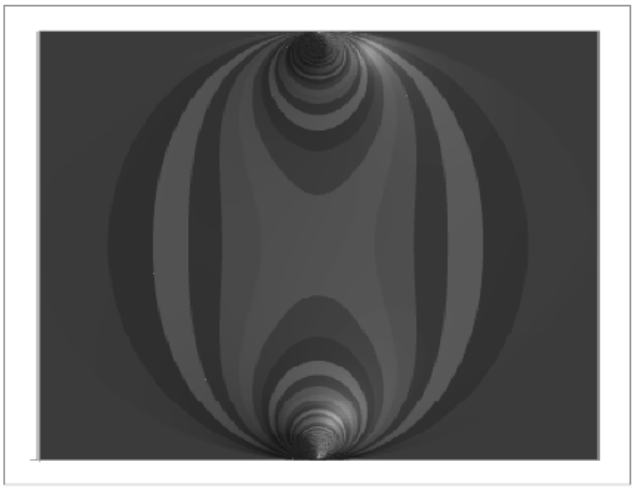

Figure 3. Analytical solution of δ^e for a disc on compression, using Eq. (11). The color change over a range of 2π radians in order to simulate the formation of fringes (Phase maps of isochromatics).

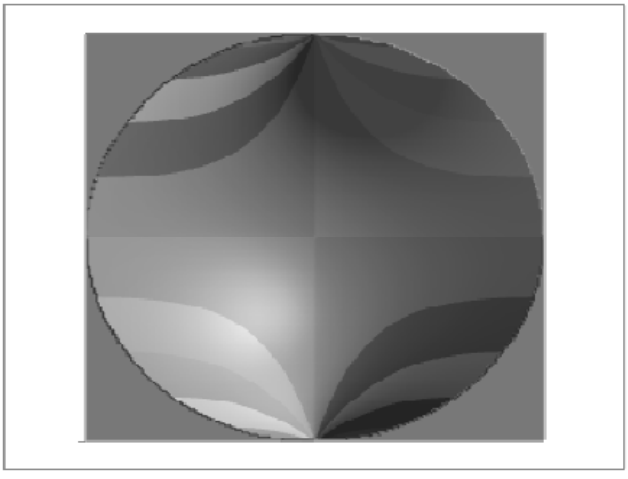

Figure 4. Analytical solution of α^e for a disc on compression, using Eq. (12). The color change over a range of 0.5 radians in order to simulate the formation of fringes (Phase maps of isoclinics).

$$\alpha = \frac{1}{2}\tan^{-1}\left(\frac{\sqrt{\begin{matrix} b_{1,1}I_1^2 & +b_{1,2}I_1I_2 & +b_{1,3}I_1I_3 & +b_{1,4}I_1I_4 & \dots & +b_{1,N}I_1I_N \\ & +b_{2,2}I_2^2 & +b_{2,3}I_2I_3 & +b_{2,4}I_2I_4 & \dots & +b_{2,N}I_2I_N \\ & & +b_{3,3}I_3^2 & +b_{3,4}I_3I_4 & \dots & +b_{3,N}I_3I_N \\ & & & +b_{4,4}I_4^2 & \dots & +b_{4,N}I_4I_N \\ & & & & \dots & \dots \\ & & & & & +b_{N,N}I_N^2 \end{matrix}}}{\sqrt{\begin{matrix} c_{1,1}I_1^2 & +c_{1,2}I_1I_2 & +c_{1,3}I_1I_3 & +c_{1,4}I_1I_4 & \dots & +c_{1,N}I_1I_N \\ & +c_{2,2}I_2^2 & +c_{2,3}I_2I_3 & +c_{2,4}I_2I_4 & \dots & +c_{2,N}I_2I_N \\ & & +c_{3,3}I_3^2 & +c_{3,4}I_3I_4 & \dots & +c_{3,N}I_3I_N \\ & & & +c_{4,4}I_4^2 & \dots & +c_{4,N}I_4I_N \\ & & & & \dots & \dots \\ & & & & & +c_{N,N}I_N^2 \end{matrix}}}\right) \quad (15)$$

$$\delta = \tan^{-1}\left(\frac{\sqrt{\begin{matrix} e_{1,1}I_1^2 & +e_{1,2}I_1I_2 & +e_{1,3}I_1I_3 & +e_{1,4}I_1I_4 & \dots & +e_{1,N}I_1I_N \\ & +e_{2,2}I_2^2 & +e_{2,3}I_2I_3 & +e_{2,4}I_2I_4 & \dots & +e_{2,N}I_2I_N \\ & & +e_{3,3}I_3^2 & +e_{3,4}I_3I_4 & \dots & +e_{3,N}I_3I_N \\ & & & +e_{4,4}I_4^2 & \dots & +e_{4,N}I_4I_N \\ & & & & \dots & \dots \\ & & & & & +e_{N,N}I_N^2 \end{matrix}}}{\sqrt{\begin{matrix} f_{1,1}I_1^2 & +f_{1,2}I_1I_2 & +f_{1,3}I_1I_3 & +f_{1,4}I_1I_4 & \dots & +f_{1,N}I_1I_N \\ & +f_{2,2}I_2^2 & +f_{2,3}I_2I_3 & +f_{2,4}I_2I_4 & \dots & +f_{2,N}I_2I_N \\ & & +f_{3,3}I_3^2 & +f_{3,4}I_3I_4 & \dots & +f_{3,N}I_3I_N \\ & & & +f_{4,4}I_4^2 & \dots & +f_{4,N}I_4I_N \\ & & & & \dots & \dots \\ & & & & & +f_{N,N}I_N^2 \end{matrix}}}\right) \quad (16)$$

In contrast, emphasizing only the matrix of coefficients of the numerator and the denominator:

$$\alpha = \frac{1}{2}\tan^{-1}\frac{\sqrt{|Num_\alpha|}}{\sqrt{|Den_\alpha|}} \quad \begin{cases} Num_\alpha = \begin{bmatrix} b_{1,1} & b_{1,2} & b_{1,3} & b_{1,4} & \dots & b_{1,N} \\ & b_{2,2} & b_{2,3} & b_{2,4} & \dots & b_{2,N} \\ & & b_{3,3} & b_{3,4} & \dots & b_{3,N} \\ & & & b_{4,4} & \dots & b_{4,N} \\ & & & & \dots & \dots \\ & & & & & b_{N,N} \end{bmatrix} \\ Den_\alpha = \begin{bmatrix} c_{1,1} & c_{1,2} & c_{1,3} & c_{1,4} & \dots & c_{1,N} \\ & c_{2,2} & c_{2,3} & c_{2,4} & \dots & c_{2,N} \\ & & c_{3,3} & c_{3,4} & \dots & c_{3,N} \\ & & & c_{4,4} & \dots & c_{4,N} \\ & & & & \dots & \dots \\ & & & & & c_{N,N} \end{bmatrix} \end{cases} \quad (17)$$

$$\delta = \tan^{-1}\frac{\sqrt{|Num_\delta|}}{\sqrt{|Den_\delta|}} \quad \begin{cases} Num_\delta = \begin{bmatrix} e_{1,1} & e_{1,2} & e_{1,3} & e_{1,4} & \dots & e_{1,N} \\ & e_{2,2} & e_{2,3} & e_{2,4} & \dots & e_{2,N} \\ & & e_{3,3} & e_{3,4} & \dots & e_{3,N} \\ & & & e_{4,4} & \dots & e_{4,N} \\ & & & & \dots & \dots \\ & & & & & e_{N,N} \end{bmatrix} \\ Den_\delta = \begin{bmatrix} f_{1,1} & f_{1,2} & f_{1,3} & f_{1,4} & \dots & f_{1,N} \\ & f_{2,2} & f_{2,3} & f_{2,4} & \dots & f_{2,N} \\ & & f_{3,3} & f_{3,4} & \dots & f_{3,N} \\ & & & f_{4,4} & \dots & f_{4,N} \\ & & & & \dots & \dots \\ & & & & & f_{N,N} \end{bmatrix} \end{cases} \quad (18)$$

The display of the phase calculation equation in this way permits the viewing of symmetries and the sparse matrix. The use of the absolute value in the numerator and the denominator restricts the angle between 0 and $\pi/2$ radians, but avoids negative roots and also eliminates false angles. Subsequent considerations will later remove this restriction.

The shift from obtaining equations for calculating the phase analytically to obtaining them numerically is a significant innovation. It breaks a paradigm that was hitherto used by several authors. After several attempts at numerical modeling of the problem, the following mathematical problem was identified (Eq. (19)):

$$Maximize \quad \sum_{r=1}^{N}\sum_{s=r}^{N}\left(b_{r,s}+c_{r,s}+e_{r,s}+f_{r,s}\right)$$

*s*ubject to

$$\begin{cases} \text{tan(angle)} = \text{Sqrt(|Num|)/Sqrt(|Den|)} \qquad \text{Quantities} \\ 1)\ \tan^2(2\alpha^v)\left(\sum_{r=1}^{N}\sum_{s=r}^{N}\left(c_{r,s}I_r^vI_s^v\right)\right) = \sum_{r=1}^{N}\sum_{s=r}^{N}\left(b_{r,s}I_r^vI_s^v\right) \quad v=1..[N(N+1)] \\ 2)\ \tan^2(\delta^v)\left(\sum_{r=1}^{N}\sum_{s=r}^{N}\left(f_{r,s}I_r^vI_s^v\right)\right) = \sum_{r=1}^{N}\sum_{s=r}^{N}\left(e_{r,s}I_r^vI_s^v\right) \quad v=1..[N(N+1)] \\ 3)\ -1\le b_{r,s}\le 1,\quad -1\le c_{r,s}\le 1 \qquad r=1..N, s=r..N \\ \quad\ -1\le e_{r,s}\le 1,\quad -1\le f_{r,s}\le 1 \qquad r=1..N, s=r..N \\ 4)\ b_{r,s},\ c_{r,s} \text{ are real numbers} \qquad r=1..N, s=r..N \\ \quad\ e_{r,s},\ f_{r,s} \text{ are real numbers} \qquad r=1..N, s=r..N \end{cases}$$

where for each v:

$$\begin{cases} I_j^v = K^v\left[1-\cos(2\theta_j)\cos(\delta^v)-\cos(2\alpha^v)\sin(2\theta_j)\sin(\delta^v)\right],\ j=1..N \\ K^v \in [0;\ 255] \quad \textit{r}\text{andom and real} \\ \alpha^v \in [0;\ \pi/4] \quad \textit{r}\text{andom and real} \\ \delta^v \in [0;\ \pi/2] \quad \textit{r}\text{andom and real} \\ \theta_j = \frac{\pi}{2}\left(\frac{j-1}{Step-1}\right)-\frac{\pi}{4},\ j=1..N \quad , \quad \theta_j \in \left[-\pi/4, \pi/4\right] \\ \Delta\theta = \frac{\pi}{2(Step-1)} \text{ radians} \end{cases}$$

Input with the integer values: $Step \ge 3$ and $N \in [3,\ Step]$

Output with the real coefficients: $b_{r,s}, c_{r,s}, e_{r,s}, f_{r,s}$, $r=1..N,\ s=r..N$ (19)

The motivation for choosing this mathematical model is the success achieved in Magalhaes, Neto and Barcellos (2010) with a similar model. The idea of the mathematical model is to maximize the coefficients ($b_{r,s}$, $c_{r,s}$, $e_{r,s}$, $f_{r,s}$) so that their values are large enough (not close to zero) to make them significant in the equation obtained. *Step* represents integer values greater than or equal to 3. *N* is the number of images, and it is an integer number between 3 and the value of *Step*.

The constraints 1 and 2 are made so that the coefficients ($b_{r,s}$, $c_{r,s}$, $e_{r,s}$, $f_{r,s}$) generate correct values for the calculation of α and δ. To ensure that one has a hyperrestricted problem, it is suggested that the number of greater restrictions must be at least equal to the number of variables.

The constraints 3 and 4 are placed on the coefficients ($b_{r,s}$, $c_{r,s}$, $e_{r,s}$, $f_{r,s}$) that are not greater than one and are not smaller than negative one, to avoid error propagation. For the needs evaluation phase, these limiting factors will increase the values of the intensity of the observations (*I*) that contains errors due to noise in the observations and excellent discretization in pixels and in shades of gray.

The ν restrictions in the model are obtained by a random choice of values for K (constant proportion of the maximum intensity of light emerging from the analyzer), δ (delay in the model given by the photoelastic isochromatic fringes) and α (angle between the direction and the axis of σ_1 horizontal reference). In fact, the values of K, δ, and α can be any real number, but to maintain compatibility with the problem, we chose to limit K between 0 and 255 so that the values of I are between 0 and 255. In addition, α is limited between 0 and $\pi/4$ radians and δ between 0 and $\pi/2$ radians so that the tangents have positive values.

The angle θ is limited to $-\pi/4$ and $\pi/4$ radians and is equally spaced when *Step* = *N*. For other values of *Step*, the angle θ starts with a value of $-\pi/4$ and is equally spaced, but it does not reach $\pi/4$. The choice of these angles is made based on the ease of calibration in the polariscope used. Other values for the angles can be used in the mathematical model.

Step must to be an integer number. The number of images (*N*) should range from 3 to the value of *Step*. *Step* is used to vary the angle with constant spacing in the polariscope analyzer. For example, for 8 images (*N* = 8) and *Step* = 10, the angles of the analyzer polariscope (θ) are as follows: –45º, –35º, –25º, –15º, –5º, 5º, 15º, and 25º.

The mathematical model is easy to solve because it involves linear programming and a maximum global solution can be obtained using the Simplex method. The processing time for the solution of this mathematical model is very fast, a few seconds on personal computers.

For example, when *N* = 3 and *Step* = 3, the angles of the polariscope analyzer (θ) are –45º, 0º, and 45º. The equations obtained with the mathematical model are shown in Eq. (20) and Eq. (21).

$$\alpha = \frac{1}{2}\tan^{-1}\left(\frac{\sqrt{\begin{matrix}-0.25I_1^2 & +I_1I_2 & +0.5I_1I_3\\ & -I_2^2 & +I_2I_3\\ & & -0.25I_3^2\end{matrix}}}{\sqrt{\begin{matrix}0.25I_1^2 & -0.5I_1I_3\\ & +0.25I_3^2\end{matrix}}}\right) \tag{20}$$

$$\delta = \tan^{-1}\left(\frac{\sqrt{\begin{matrix}I_1I_2\\ -I_2^2 & +I_2I_3\end{matrix}}}{\sqrt{\begin{matrix}0.25I_1^2 & -I_1I_2 & +0.5I_1I_3\\ & +I_2^2 & -I_2I_3\\ & & +0.25I_3^2\end{matrix}}}\right) \tag{21}$$

In another example, when *N* = 4 and *Step* = 4, the angles of the polariscope analyzer (θ) are –45º, –15º, 15º, and 45º. The equations obtained with the mathematical model are shown in Eq. (22) and Eq. (23).

$$\alpha = \frac{1}{2}\tan^{-1}\left(\frac{\sqrt{\begin{matrix}-0.375I_1^2 & +I_1I_2 & +I_1I_3 & +0.25I_1I_4\\ & -I_2^2 & & +I_2I_4\\ & & -I_3^2 & +I_3I_4\\ & & & -0.375I_4^2\end{matrix}}}{\sqrt{\begin{matrix}-0.25I_1^2 & +I_1I_2 & -I_1I_3 & +0.5I_1I_4\\ & +0.5I_2^2 & -I_2I_3 & -I_2I_4\\ & & +0.5I_3^2 & +I_3I_4\\ & & & -0.25I_4^2\end{matrix}}}\right) \tag{22}$$

$$\delta = \tan^{-1}\left(\frac{\sqrt{\begin{matrix}-0.125I_1^2 & +I_1I_2 & +I_1I_3 & -0.25I_1I_4\\ & -0.5I_2^2 & -I_2I_3 & +I_2I_4\\ & & -0.5I_3^2 & +I_3I_4\\ & & & -0.125I_4^2\end{matrix}}}{\sqrt{\begin{matrix}0.5I_1^2 & -I_1I_2 & -I_1I_3 & +I_1I_4\\ & +0.5I_2^2 & +I_2I_3 & -I_2I_4\\ & & +0.5I_3^2 & -I_3I_4\\ & & & +0.5I_4^2\end{matrix}}}\right) \tag{23}$$

In another example, when *N* = 3 and *Step* = 4, the angles of the polariscope analyzer (θ) are –45º, –15º, and 15º. The equations obtained with the mathematical model are shown in Eq. (24) and Eq. (25).

$$\alpha = \frac{1}{2}\tan^{-1}\left(\frac{\sqrt{\begin{matrix}-(1/9)I_1^2 & +(2/3)I_1I_2 & +(2/9)I_1I_3\\ & -I_2^2 & +(2/3)I_2I_3\\ & & -(1/9)I_3^2\end{matrix}}}{\sqrt{\begin{matrix}+(1/3)I_2^2 & -(2/3)I_2I_3\\ & +(1/3)I_3^2\end{matrix}}}\right) \tag{24}$$

$$\delta = \tan^{-1}\left(\frac{\sqrt{\begin{matrix}-(5/6)I_1^2 & +(1/2)I_1I_2 & +(1/6)I_1I_3\\ & -(1/2)I_2^2 & \\ & & +(1/6)I_3^2\end{matrix}}}{\sqrt{\begin{matrix}(1/3)I_1^2 & -I_1I_2 & +(1/3)I_1I_3\\ & +(3/4)I_2^2 & -(1/2)I_2I_3\\ & & +(5/6)I_3^2\end{matrix}}}\right) \tag{25}$$

In a different example, when *N* = 7 and *Step* = 7, the angles of the polariscope analyzer (θ) are –45º, –30º, –15º, 0º, 15º, 30º, and 45º. Here the differences are in coefficients being integers instead of real; this was done by changing the mathematical model for integer programming. The equations obtained with the mathematical model are shown in Eq. (26) and Eq. (27).

$$\alpha = \frac{1}{2}\tan^{-1}\left(\frac{\sqrt{\begin{matrix}-2I_1^2 & +2I_1I_3 & +2I_1I_4 & +2I_1I_5 & & +2I_1I_7\\ & +I_2^2 & +I_2I_3 & -I_2I_4 & +I_2I_5 & +I_2I_6 & \\ & & -2I_3^2 & -I_3I_4 & -I_3I_5 & +I_3I_6 & +2I_3I_7\\ & & & -2I_4^2 & -I_4I_5 & -I_4I_6 & +2I_4I_7\\ & & & & -2I_5^2 & +I_5I_6 & +2I_5I_7\\ & & & & & +I_6^2 & \\ & & & & & & -2I_7^2\end{matrix}}}{\sqrt{\begin{matrix}I_1^2 & -I_1I_3 & +2I_1I_4 & -I_1I_5 & & -I_1I_7\\ & & & & -2I_2I_6 & \\ & +2I_3^2 & & -2I_3I_5 & & -I_3I_7\\ & & -I_4^2 & & & +2I_4I_7\\ & & & +2I_5^2 & & -I_5I_7\\ & & & & & \\ & & & & & +I_7^2\end{matrix}}}\right) \tag{26}$$

$$\delta = \tan^{-1}\left(\frac{\begin{vmatrix} -2I_1^2 & +2I_1I_2 & +2I_1I_3 & & +2I_1I_5 & +2I_1I_6 & -2I_1I_7 \\ & +2I_2^2 & & -2I_2I_4 & & & +2I_2I_7 \\ & & -2I_3^2 & & & & +2I_3I_7 \\ & & & -I_4^2 & & -2I_4I_6 & \\ & & & & -2I_5^2 & & +2I_5I_7 \\ & & & & & +2I_6^2 & +2I_6I_7 \\ & & & & & & -2I_7^2 \end{vmatrix}}{\begin{vmatrix} 2I_1^2 & -2I_1I_3 & -2I_1I_4 & -2I_1I_5 & & +2I_1I_7 \\ -I_2^2 & & & & +2I_2I_6 & \\ & +2I_3^2 & & & & -2I_3I_7 \\ & & +2I_4^2 & & & -2I_4I_7 \\ & & & +2I_5^2 & & -2I_5I_7 \\ & & & & -I_6^2 & \\ & & & & & +2I_7^2 \end{vmatrix}}\right) \quad (27)$$

For example, with 10 images (N = 10) and *Step* = 10, the angles of the analyzer polariscope (θ) are as follows ($\Delta\theta$ = 10º): θ_1 = –45º, θ_2 = –35º, θ_3 = –25º, θ_4 = –15º, θ_5 = –5º, θ_6 = 5º, θ_7 = 15º, θ_8 = 25º, θ_9 = 35º, and θ_{10} = 45º. The equations obtained with the mathematical model are shown in Table 1 with values of the coefficients ($b_{r,s}$, $c_{r,s}$, $e_{r,s}$, $f_{r,s}$).

For example, with N = 11 and *Step* = 11, the angles of the analyzer polariscope (θ) are as follows ($\Delta\theta$ = 9º): θ_1 = –45º, θ_2 = –36º, θ_3 = –27º, θ_4 = –18º, θ_5 = –9º, θ_6 = 0º, θ_7 = 9º, θ_8 = 18º, θ_9 = 27º, θ_{10} = 36º, and θ_{11} = 45º. The equations obtained with the mathematical model are shown in Table 2 with values of the coefficients ($b_{r,s}$, $c_{r,s}$, $e_{r,s}$, $f_{r,s}$). The coefficients are displayed with 5 decimal places, but were calculated in 19 decimal places of accuracy. These values are shown for purposes of direct use of the new equations and conference implementation of the mathematical model.

Table 1. Values of the real coefficients ($b_{r,s}$, $c_{r,s}$, $e_{r,s}$, $f_{r,s}$), when N = 10 and *Step* = 10.

Index	$b_{r,s}$	$c_{r,s}$	$e_{r,s}$	$f_{r,s}$	Index	$b_{r,s}$	$c_{r,s}$	$e_{r,s}$	$f_{r,s}$
r=1 ; s=1	-1.00000	-1.00000	-1.00000	1.00000	r=4 ; s=4	-1.00000	-1.00000	-1.00000	1.00000
r=1 ; s=2	-1.00000	1.00000	-0.87367	1.00000	r=4 ; s=5	-1.00000	-1.00000	-1.00000	1.00000
r=1 ; s=3	1.00000	1.00000	1.00000	0.91797	r=4 ; s=6	-1.00000	-1.00000	-1.00000	1.00000
r=1 ; s=4	1.00000	1.00000	1.00000	-1.00000	r=4 ; s=7	-1.00000	1.00000	-1.00000	1.00000
r=1 ; s=5	1.00000	1.00000	1.00000	-1.00000	r=4 ; s=8	-0.03206	-1.00000	1.00000	1.00000
r=1 ; s=6	1.00000	-1.00000	-1.00000	-1.00000	r=4 ; s=9	1.00000	-1.00000	1.00000	-1.00000
r=1 ; s=7	1.00000	1.00000	1.00000	-1.00000	r=4 ; s=10	1.00000	-1.00000	-0.35622	-1.00000
r=1 ; s=8	1.00000	-0.12390	1.00000	1.00000	r=5 ; s=5	-1.00000	-1.00000	-1.00000	1.00000
r=1 ; s=9	0.56382	-1.00000	1.00000	1.00000	r=5 ; s=6	-1.00000	1.00000	-1.00000	1.00000
r=1 ; s=10	-1.00000	-1.00000	-1.00000	1.00000	r=5 ; s=7	-1.00000	1.00000	-1.00000	1.00000
r=2 ; s=2	-0.87625	0.72262	1.00000	1.00000	r=5 ; s=8	-1.00000	-0.84173	0.29954	-1.00000
r=2 ; s=3	1.00000	1.00000	1.00000	-1.00000	r=5 ; s=9	1.00000	1.00000	1.00000	-1.00000
r=2 ; s=4	1.00000	-1.00000	1.00000	-1.00000	r=5 ; s=10	1.00000	-1.00000	1.00000	-1.00000
r=2 ; s=5	1.00000	-1.00000	1.00000	-1.00000	r=6 ; s=6	-1.00000	1.00000	-1.00000	1.00000
r=2 ; s=6	1.00000	-1.00000	-1.00000	-1.00000	r=6 ; s=7	-1.00000	-1.00000	-1.00000	1.00000
r=2 ; s=7	1.00000	1.00000	1.00000	-1.00000	r=6 ; s=8	-1.00000	-1.00000	1.00000	-0.95811
r=2 ; s=8	1.00000	-1.00000	1.00000	-1.00000	r=6 ; s=9	1.00000	-0.75947	1.00000	-1.00000
r=2 ; s=9	1.00000	-1.00000	1.00000	1.00000	r=6 ; s=10	1.00000	-1.00000	1.00000	-1.00000
r=2 ; s=10	1.00000	1.00000	-1.00000	1.00000	r=7 ; s=7	-1.00000	1.00000	-1.00000	1.00000
r=3 ; s=3	1.00000	1.00000	1.00000	-1.00000	r=7 ; s=8	-1.00000	1.00000	1.00000	1.00000
r=3 ; s=4	-1.00000	1.00000	0.61212	-1.00000	r=7 ; s=9	1.00000	1.00000	1.00000	-1.00000
r=3 ; s=5	-1.00000	-1.00000	-1.00000	-1.00000	r=7 ; s=10	1.00000	1.00000	1.00000	-1.00000
r=3 ; s=6	-1.00000	-0.67863	-1.00000	0.42187	r=8 ; s=8	1.00000	1.00000	-0.84213	0.35815
r=3 ; s=7	0.52638	1.00000	-1.00000	1.00000	r=8 ; s=9	1.00000	0.68111	-1.00000	-1.00000
r=3 ; s=8	1.00000	1.00000	1.00000	1.00000	r=8 ; s=10	1.00000	-1.00000	1.00000	-1.00000
r=3 ; s=9	1.00000	1.00000	1.00000	-0.73988	r=9 ; s=9	-0.81120	1.00000	-1.00000	1.00000
r=3 ; s=10	1.00000	-1.00000	-1.00000	-1.00000	r=9 ; s=10	-1.00000	-1.00000	1.00000	1.00000
					r=10 ; s=10	-1.00000	1.00000	-0.61617	1.00000

Thus, for each value of *Step* greater than or equal to 3 and N between 3 and the value of *Step*, the mathematical model of Eq. 19 provides values of the real coefficients ($b_{r,s}$, $c_{r,s}$, $e_{r,s}$, $f_{r,s}$), which represents an unprecedented and new phase equation for α and δ.

Because the new equations were developed from the algorithms, a numerical calculation, rather than an analytical demonstration of trigonometric relations, is necessary to check them. It is believed that a large number of numerical tests can validate or verify these new equations or at least minimize the chance of these equations being wrong or false. To test the usefulness of the new equations for calculating the phase, a computer program was created, which generated random values of $K \in [0, 255]$, $\alpha' \in [0, \pi/4]$, and $\delta' \in [0, \pi/2]$. Using Eq. (3), the program calculates N values of I_j, one for each value of θ_j. With the values of I_j, the new phase equations were applied and tested to determine whether they produced the correct values of α and δ. The values of I_j (luminous intensity of the image) are calculated with j ranging from 1 to N. The new equations with the values of I_j are applied, giving a tan (α) and a tan (δ) that must be compared with the value of randomly assigned (α' and δ')

values. This comparison involves the accuracy of a very small value because of the number of rounding errors that can occur in the calculations, that is, the precision ($|\alpha' - \alpha| + |\delta' - \delta| \leq 10^{-6}$. This calculation was performed thousands of times (at least 100.000 times) for each equation in the phase calculation. It was generated at least 99.999% of the time with an accuracy of 10^{-6}. The mathematical model of Eq. (19) was successfully tested until *Step* and *N* equal 1801, the value at which the increment $\Delta\theta$ would be 0.05°. Thus, it was believed that the chances for the equations to be wrong or false have been minimized.

Before Unwrapping, Change to [-π, π]

Because of the character of the evaluation equations, only phase values $\alpha \in [0, \pi/4]$ and $\delta \in [0, \pi/2]$ radians were calculated. For unequivocal determination of the wrapped phase value angles $\in [-\pi, \pi]$ it was necessary to test values δ, $-\delta$, $\delta-\pi$, and $-\delta+\pi$ by combining them with α, $-\alpha$, $\alpha-\pi$, and $-\alpha+\pi$ using values of I_j and small systems in Eq. (28). The values were tested based on the symmetries of the tangent function. Sixteen tests were performed, and the correct values of α and δ were sought between -π and π, because the experimental values I_j and θ_j are known (Arellano, 2008).

$$\begin{cases} I_1 = K\left[1-\cos(2\theta_1)\cos(\delta)-\cos(2\alpha)\sin(2\theta_1)\sin(\delta)\right] \\ I_2 = K\left[1-\cos(2\theta_2)\cos(\delta)-\cos(2\alpha)\sin(2\theta_2)\sin(\delta)\right] \\ \qquad\qquad\qquad\qquad \cdots \\ I_N = K\left[1-\cos(2\theta_N)\cos(\delta)-\cos(2\alpha)\sin(2\theta_N)\sin(\delta)\right] \end{cases} \qquad (28)$$

We obtain α and δ between [-π, π]. The next step is to unwrap the wrapped phase map. When unwrapping, several of the phase values should be shifted by an integer multiple of 2π. Unwrapping is thus adding or subtracting 2π offsets at each discontinuity encountered in the phase data. The unwrapping procedure consists in finding the correct field number for each phase measurement (Estrada, Servin and Quiroga, 2011; Navarro et al., 2012).

Table 2. Values of the real coefficients ($b_{r,s}$, $c_{r,s}$, $e_{r,s}$, $f_{r,s}$), when N = 11 and *Step* = 11.

Index	$b_{r,s}$	$c_{r,s}$	$e_{r,s}$	$f_{r,s}$
r=1 ; s=1	-1.00000	1.00000	-0.84196	1.00000
r=1 ; s=2	-1.00000	1.00000	1.00000	1.00000
r=1 ; s=3	1.00000	-1.00000	-1.00000	1.00000
r=1 ; s=4	1.00000	-1.00000	-1.00000	-1.00000
r=1 ; s=5	1.00000	-1.00000	1.00000	-1.00000
r=1 ; s=6	1.00000	-0.17627	1.00000	-1.00000
r=1 ; s=7	1.00000	1.00000	0.51373	-1.00000
r=1 ; s=8	1.00000	-1.00000	1.00000	-1.00000
r=1 ; s=9	1.00000	-1.00000	1.00000	1.00000
r=1 ; s=10	-0.22709	-1.00000	-1.00000	1.00000
r=1 ; s=11	-1.00000	-1.00000	-1.00000	1.00000
r=2 ; s=2	-1.00000	1.00000	1.00000	1.00000
r=2 ; s=3	1.00000	1.00000	1.00000	-0.43243
r=2 ; s=4	1.00000	1.00000	1.00000	-1.00000
r=2 ; s=5	1.00000	1.00000	-1.00000	-1.00000
r=2 ; s=6	1.00000	-1.00000	1.00000	-1.00000
r=2 ; s=7	1.00000	0.36529	1.00000	-1.00000
r=2 ; s=8	1.00000	1.00000	-1.00000	-1.00000
r=2 ; s=9	1.00000	1.00000	1.00000	-1.00000
r=2 ; s=10	1.00000	1.00000	1.00000	1.00000
r=2 ; s=11	0.42352	-1.00000	-1.00000	1.00000
r=3 ; s=3	0.74631	1.00000	1.00000	-1.00000
r=3 ; s=4	-1.00000	-1.00000	1.00000	-1.00000
r=3 ; s=5	-1.00000	-1.00000	-1.00000	-1.00000
r=3 ; s=6	-0.36945	1.00000	-1.00000	-1.00000
r=3 ; s=7	1.00000	1.00000	1.00000	1.00000
r=3 ; s=8	1.00000	1.00000	1.00000	0.86665
r=3 ; s=9	1.00000	-1.00000	1.00000	-1.00000
r=3 ; s=10	1.00000	-1.00000	1.00000	1.00000
r=3 ; s=11	1.00000	-1.00000	-1.00000	0.66946
r=4 ; s=4	-1.00000	-1.00000	0.89444	1.00000
r=4 ; s=5	-1.00000	-1.00000	-1.00000	1.00000
r=4 ; s=6	-1.00000	1.00000	-1.00000	1.00000
r=4 ; s=7	-1.00000	-1.00000	-1.00000	1.00000
r=4 ; s=8	-1.00000	-1.00000	-0.04016	1.00000
r=4 ; s=9	1.00000	-1.00000	1.00000	-1.00000
r=4 ; s=10	1.00000	-1.00000	1.00000	-1.00000
r=4 ; s=11	1.00000	-1.00000	1.00000	-1.00000
r=5 ; s=5	-1.00000	1.00000	-1.00000	1.00000
r=5 ; s=6	-1.00000	0.42636	-1.00000	1.00000
r=5 ; s=7	-1.00000	-0.49046	-1.00000	1.00000
r=5 ; s=8	-1.00000	1.00000	-1.00000	1.00000
r=5 ; s=9	1.00000	1.00000	1.00000	-1.00000
r=5 ; s=10	1.00000	1.00000	-0.59913	-1.00000
r=5 ; s=11	1.00000	-1.00000	1.00000	-1.00000
r=6 ; s=6	-1.00000	-1.00000	-1.00000	1.00000
r=6 ; s=7	-1.00000	-1.00000	-1.00000	1.00000
r=6 ; s=8	-1.00000	1.00000	-1.00000	1.00000
r=6 ; s=9	-0.91620	1.00000	0.25454	-1.00000
r=6 ; s=10	1.00000	1.00000	1.00000	-1.00000
r=6 ; s=11	1.00000	1.00000	1.00000	-1.00000
r=7 ; s=7	-1.00000	-0.89426	-1.00000	1.00000
r=7 ; s=8	-1.00000	1.00000	-1.00000	1.00000
r=7 ; s=9	-1.00000	-1.00000	1.00000	0.78597
r=7 ; s=10	1.00000	-1.00000	1.00000	-1.00000
r=7 ; s=11	1.00000	1.00000	1.00000	-1.00000
r=8 ; s=8	-1.00000	1.00000	-1.00000	1.00000
r=8 ; s=9	-1.00000	-1.00000	-1.00000	-1.00000
r=8 ; s=10	1.00000	-1.00000	-1.00000	-1.00000
r=8 ; s=11	1.00000	1.00000	1.00000	-1.00000
r=9 ; s=9	1.00000	-1.00000	1.00000	-1.00000
r=9 ; s=10	1.00000	1.00000	1.00000	-0.88966
r=9 ; s=11	1.00000	0.76934	1.00000	1.00000
r=10 ; s=10	-1.00000	1.00000	-1.00000	1.00000
r=10 ; s=11	-1.00000	-1.00000	1.00000	1.00000
r=11 ; s=11	-1.00000	1.00000	-1.00000	1.00000

Testing and Analysis of Error

To assess the practical use of the method developed in this work, a stress-frozen disk under diametric compression, D = 100.0 mm in diameter, H = 5.0 mm thick and made of epoxy, is used. The pixel numbers, which are used for digitization, are 1024 × 1024. The grey level of each pixel ranges from 0 to 255. The light source used in this experiment is white light from a sodium lamp. Figure 5 shows diagram of the assembly of experiments with the polariscope where only the analyzer is rotated (change the angle on each photo). Flowchart of processing applied to phase-shifting method in digital photoelasticity is show in the Fig. 6.

The Figure 7 shows isochromatic fringe orders of the experimental solution with new method. The fringe orders (n) are calculated by Eq. (29). Note in the picture the presence of noise and defects due to imperfections of the photographs taken of the photoelastic model (Wijerathne, Oguni and Hori, 2008). The problem consists in the photographs having a high rate of noise, imperfections and uncertainties due to dust in the air; the whole optical polariscope and camera lens, even after cleaning the equipment before testing; mechanical vibration in the laboratory; the variations in room temperature; the reflected light, because the laboratory was not completely dark; the errors in the phase shift of images due to reduction of the areas to be analyzed; error in the positioning of optical elements, in relation to the light source, specimen and the camera, which should be exactly linear in the center; error in measuring the diameter and thickness of the specimen; error of measurement of the load by the load cell, and errors in the discretization image points and grayscale. Several sources of errors and uncertainties in photoelastic experiments are cited in Ashokan and Ramesh (2009).

$$n = \frac{H}{F}(\sigma_1 - \sigma_2) \tag{29}$$

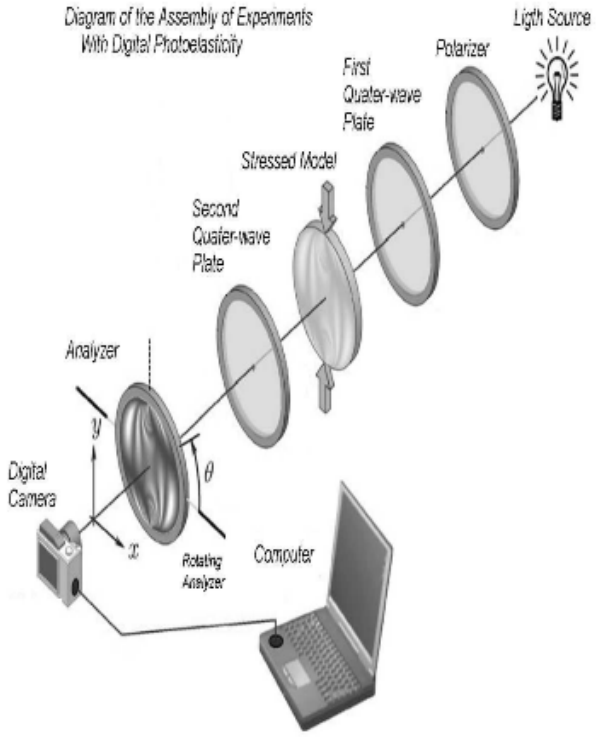

Figure 5. Arrangement of the experiments (circular polariscope) with the new method proposed.

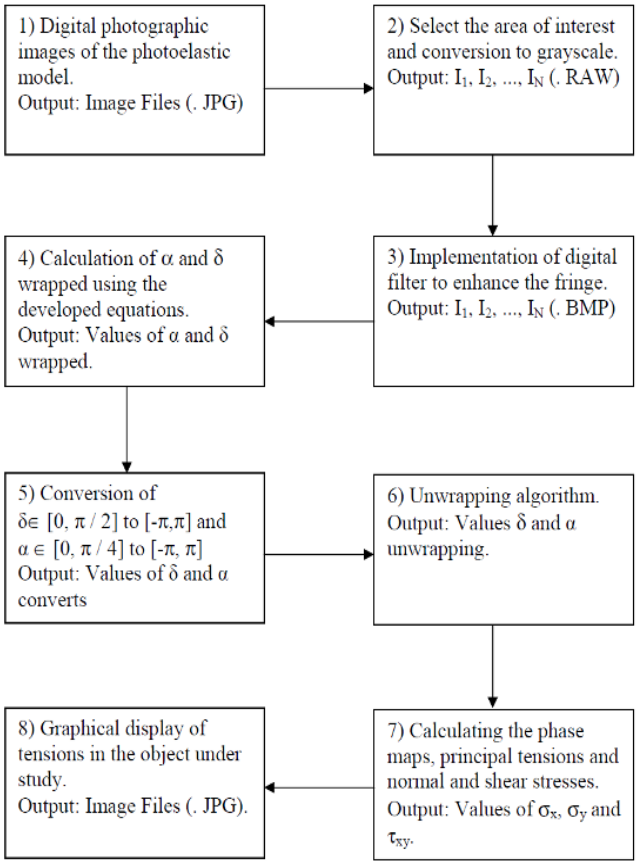

Figure 6. Flowchart of processing with the outputs and results of each stage.

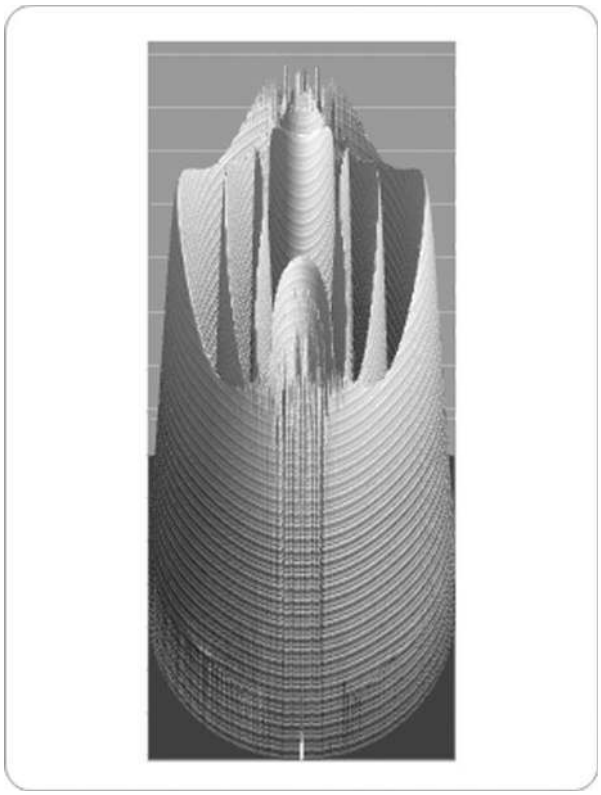

Figure 7. Fringe orders (n) obtained from experimental measurements.

To test the new equations for the phase calculation, they were used with the technique of photoelasticity for an object with known stress and to evaluate the average error using Eq. (30) and Eq. (31). This process was started with three images, repeated with four, then five and so on. The idea was to show that with an increasing number of images, the average error tends to decrease. Figure 8 shows an example of this procedure.

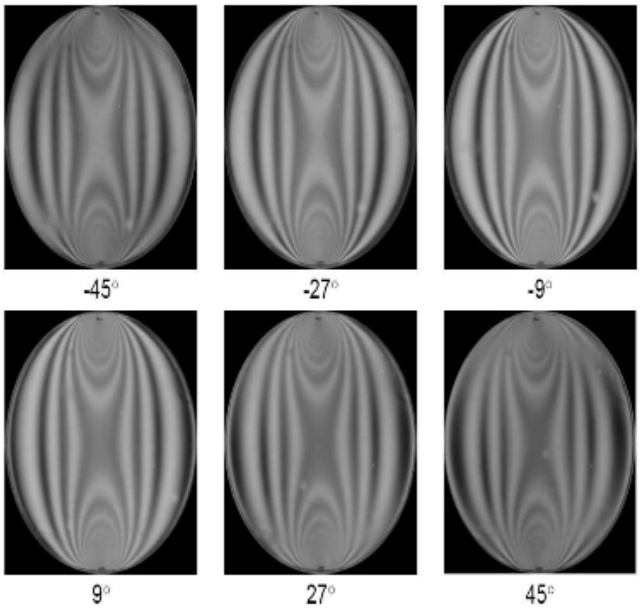

Figure 8. Set with 6 images of the photographs taken of the photoelastic model, $\Delta\theta$ equal to 18°; the disk is under compression.

$$Average \quad Error \quad for \quad \alpha \quad (E_\alpha) = \frac{1}{M}\sum_{i=1}^{M}\left|\alpha_i^e - \alpha_i\right| \qquad (30)$$

$$Average \quad Error \quad for \quad \delta \quad (E_\delta) = \frac{1}{M}\sum_{i=1}^{M}\left|\delta_i^e - \delta_i\right| \qquad (31)$$

where M is the number of pixels of the image and α_i^e and δ_i^e are the exact values calculated by Eqs. (6)-(12) for the disk. The values of α_i and δ_i are calculated by the new equation. In the analysis of the error, only the zones within the photos that were unambiguous and contained no inconsistencies were considered (Ashokan and Ramesh, 2009).

To compare the new equations for calculating the phase, nine sets of photos with *Step* set to 3, 4, 6, 7, 10, 11, 16, 19, and 31 were generated. In each set, the angle θ of the analyzer is varied ($\Delta\theta$): 45º, 30º, 18º, 15º, 10º, 9º, 6º, 5º, and 3º, respectively. Each set was computed using the average error of 3 to the number of *Step* images and using equations to evaluate the angles α and δ. The data are shown below in Tables 3 and 4. Figures 9 and 10 show that the average error decreases when the number of images increases. It may be noted that for a number of images, the average error increases when the variation of the angle θ between the images decreases.

It is important to note that for each equation developed, the average errors found for the angle δ are larger than the errors found for the angle α of the fringes isoclines. It is believed that this occurs because the absolute values of δ are higher than the absolute values of α.

Table 3. Average error in 10^{-6} rad versus number of frames (N) for angle α.

Average Error of the α in 10^{-6} rad	Set of Image	1	2	3	4	5	6	7	8	9
	Δθ	45º	30º	18º	15º	10º	9º	6º	5º	3º
	Step	3	4	6	7	10	11	16	19	31
Number of Image (N)	3	4712	6879	9762	11256	16786	18342	22312	27453	29601
	4		4005	6239	9562	11076	16265	18003	22201	27298
	5			3955	5945	8654	9698	12671	15643	18964
	6			3520	3645	4521	4799	5210	7564	9863
	7				3290	3489	3845	4075	6178	7843
	8					3132	3320	3821	5854	6582
	9					2985	3255	3594	5123	5987
	10					2845	2930	3278	4021	4388
	11						2602	2725	3267	3678
	12							2503	3077	3333
	13							2384	2988	3167
	14							2241	2845	3011
	15							2133	2458	2637
	16							1921	2112	2353
	17								1682	1976
	18								1378	1734
	19								1241	1667
	20									1535
	21									1402
	22									1378
	23									1320
	24									1298
	25									1204
	26									1167
	27									1076
	28									1005
	29									945
	30									806
	31									745

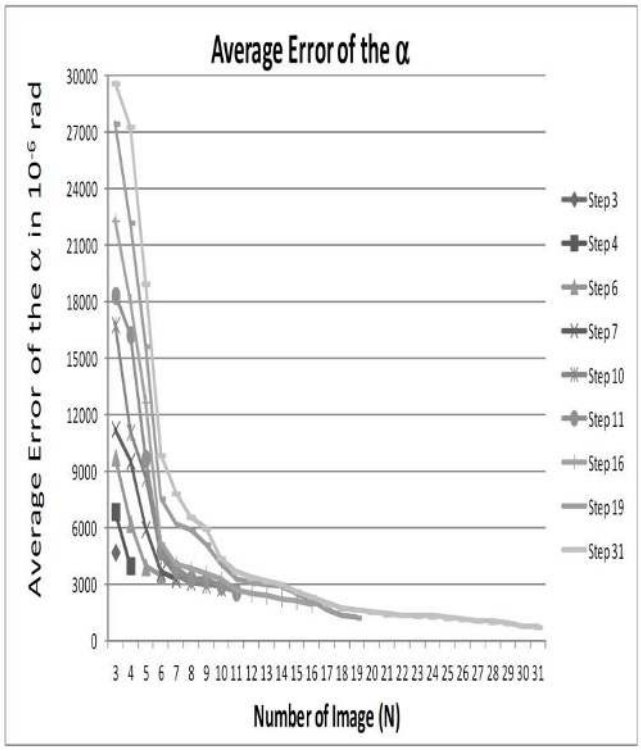

Figure 9. A plot of the data from Table 3 with the average error in 10^{-6} rad versus the number of frames (N) for angle α.

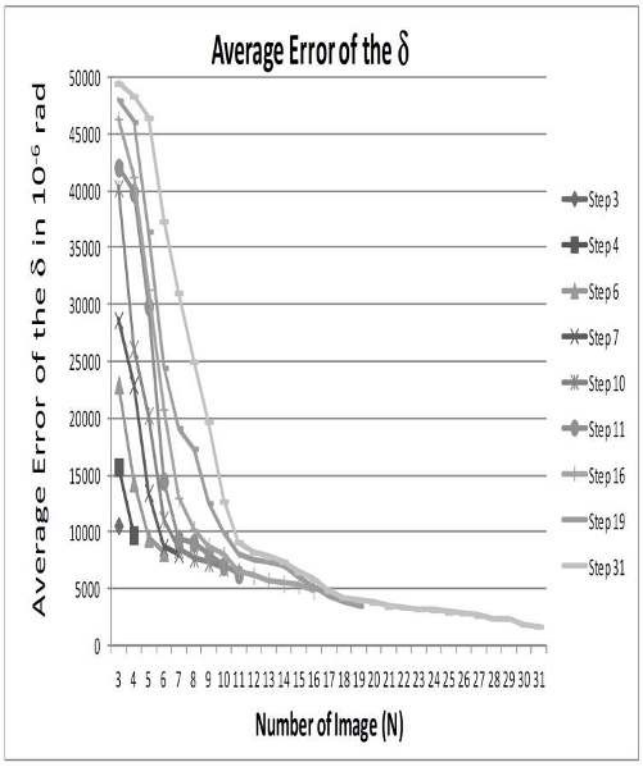

Figure 10. A plot of the data from Table 4 with the average error in 10^{-6} rad versus the number of frames (*N*) for angle δ.

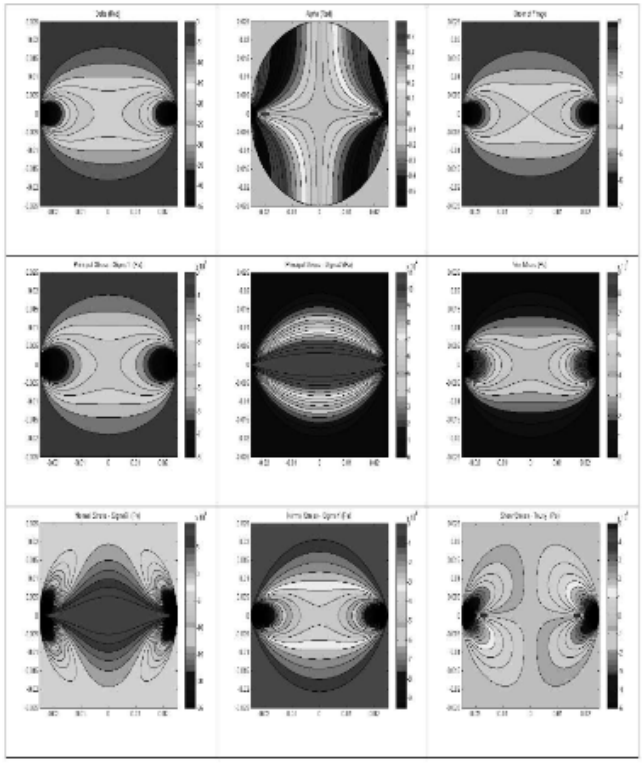

Figure 11. Results obtained through experimental measurements using the new equations with *N* = 6 and *Step* = 6 of: δ, α, fringe order(*n*), σ_1, σ_2, von Mises stress(σ_v), σ_x, σ_y and τ_{xy}.

Table 4. Average error in 10^{-6} rad versus the number of frames (*N*) for angle δ.

Average Error of the δ in 10^{-6} rad	Set of image	1	2	3	4	5	6	7	8	9
	Δθ	45º	30º	18º	15º	10º	9º	6º	5º	3º
	Step	3	4	6	7	10	11	16	19	31
Number of Image (N)	3	10577	15721	22985	28654	40250	42066	46327	47965	49443
	4		9745	14383	22952	26124	39867	41233	46076	48346
	5			9517	13469	20263	29838	31335	36435	46432
	6			8259	8679	11108	14491	20801	24452	37333
	7				8084	8473	9447	13012	19179	31055
	8					7694	9057	10271	17332	25002
	9					7301	7999	8780	12566	19710
	10					6890	7035	8017	9881	12700
	11						6293	6574	8007	9127
	12							6155	7592	8180
	13							5738	7356	7802
	14							5476	6990	7412
	15							5348	6039	6479
	16							4866	5165	5781
	17								4377	4852
	18								3880	4261
	19								3541	4032
	20									3821
	21									3442
	22									3386
	23									3240
	24									3152
	25									2958
	26									2867
	27									2644
	28									2412
	29									2366
	30									1907
	31									1717

To compare the present equations with the equations deduced by other authors, the equations were applied to the analysis of error in the algorithm of Patterson and Wang (1991). Values of $E_\alpha = 2104 \times 10^{-6}$ rad and $E_\delta = 5312 \times 10^{-6}$ rad were obtained.

For the Patterson and Wang algorithm with six images, the average error is less than six images using the new equations. It is believed that the major distinction between the pictures of the phase shifts is the reason why this improved result is obtained. However, to obtain these images, it is necessary to rotate the analyzer and the second plate of the polariscope by a quarter-wave.

The average error of the algorithm of Wang and Patterson with 6 images is in the range of the average error found for 11 images using the new equations, but for more than 16 images, lower average errors for the newly developed equations can be observed, indicating that a larger number of images yielded smaller errors. Similar results were obtained with the algorithms proposed by other authors in Ramji and Prasath (2011), Ramji and Ramesh (2008) and Chang and Wu (2011).

The significant advantage of the methodology proposed in this paper is that the method only changes the angle of the analyzer in the polariscope and that one can obtain equations for calculating the phase for any number of images in various situations.

More experiments were performed with other values of load (*P*), diameter of the disk (*D*), the disk thickness (*H*), and material fringe constant (*F*) with very similar results. These new experiments were conducted to validate and confirm the proposed method.

Figures 11 and 12 show the results obtained with the application of the new phase calculation equations developed for various values of *N* and *Step*. Note that there is little visual or graphic difference between the results obtained using the three different equations. This is due to high resolution graphics of photographic images, and

the good results achieved with the new equations developed in the research. Numerically, the equations with more images have less uncertainty and therefore, they are more accurate. Thus, there was obtained the best values of stress with number of images $N = 31$ and $Step = 31$, than using $N = 6$ and $Step = 6$.

Once obtained the value of α and δ unwrapping, apply digital implementation of the shear difference technique for whole field stress separation of 2-D problems of any geometry showed in Ramesh (2000) and Ramji and Ramesh (2008abc). Thus, it calculates the values of the phase maps, principal tensions (σ_1, σ_2) and normal (σ_x, σ_y) and shear (τ_{xy}) stresses. The von Mises stress or equivalent tensile stress (σ_v), a scalar stress value that can be computed, too. Thereafter, graphical displays of tensions in the object under study are shown.

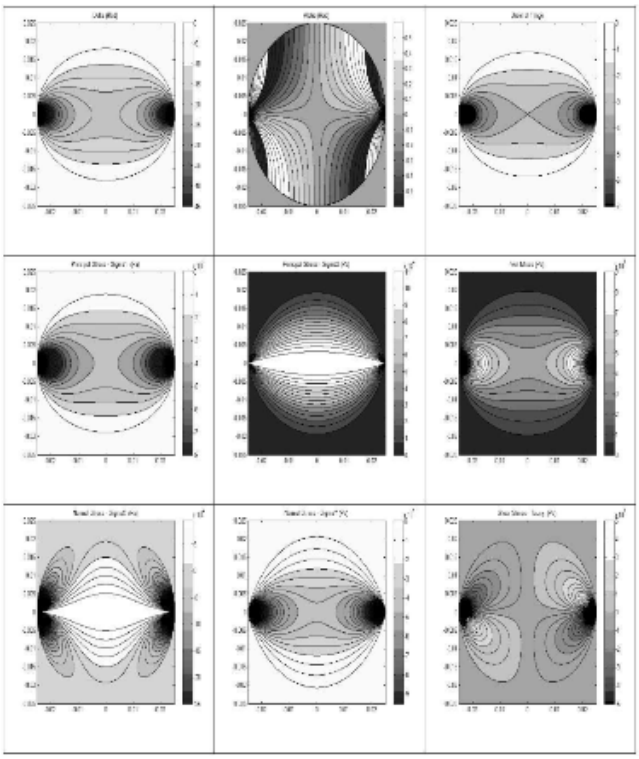

Figure 12. Results obtained through experimental measurements using the new equations with $N = 31$ and $Step = 31$ of: δ, α, fringe order(n), σ_1, σ_2, von Mises stress(σ_v), σ_x, σ_y and τ_{xy}.

Conclusion

This paper addresses the equations used for phase calculation measurements with images using phase shifting technique. The new equations are shown to be capable of processing the optical signal of photoelasticity. These techniques are very precise, easy to use, and low cost. On the basis of the performed error analysis, it can be concluded that the new equations are very good phase calculation algorithms. The metric analysis of the considered system demonstrated that its uncertainties of measurement depend on the frame period of the grid, on the resolution of photos in pixel and on the number of frames. However, the uncertainties involved in the measurement of the geometric parameters and the phase still require attention. In theory, if we have many frames, the measurement errors become very small. The measurement results obtained by the optical system demonstrate its industrial and engineering applications in experimental mechanics.

New numerical equations are deduced to calculate the directions of the tensions and delays (phase maps of the isoclines and isochromatic fringes) for the full-field image automatically, by programming the phase shift method in digital photoelasticity. With these new equations, a larger number of images phase shifted only by rotation of the analyzer can be used, and the gain can be calculated with lower uncertainties. Numerical methods were employed in an unprecedented way with the photoelastic technique to obtain a methodology for deriving the new equations. Until now, these equations were determined by algebraic and analytic methods.

With the new equations, it was possible to develop a photoelastic system that moves the analyzer of the polariscope at a constant speed while a camera takes many pictures at equal intervals of times, like a film. With this technique, the obtained measurements are more precise, and there are fewer uncertainties.

Digital photoelasticity is an important optical metrology follow-up for stress and strain analysis using full-field digital photographic images. Advances in digital image processing, data acquisition, procedures for pattern recognition and storage capacity enable use of the computer-aided technique in automation and facilitate improvement of the digital photoelastic technique. Photoelasticity has seen some renewed interest in the past few years with digital imaging, image processing and new methods becoming readily available. However, further research is needed to improve the accuracy, the precision and the automation of the photoelastic technique.

Acknowledgements

The authors thank the generous support from Pontificia Universidade Católica de Minas Gerais – PUCMINAS, Conselho Nacional de Desenvolvimento Científico e Tecnológico – CNPq, and Fundação de Amparo à Pesquisa de Minas Gerais – FAPEMIG.

References

Arellano, N.I.T., Zurita, G.R., Fabian, C.M. and Castillo, J.F.V., 2008, "Phase shifts in the Fourier spectra of phase gratings and phase grids: an application for one-shot phase-shifting interferometry", *Opt. Express*, 16, pp. 19330-19341.

Ashokan, K. and Ramesh, K., 2009, "Finite element simulation of isoclinic and isochromatic phasemaps for use in digital photoelasticity", *Experimental Techniques*, 33, pp. 38-44.

Asundi, A.K., 2002, "MATLAB for Photomechanics – A Primer", Elsevier Science.

Asundi, A.K., Tong, L. and Boay, C.G., 2001, "Dynamic Phase-Shifting Photoelasticity", *Appl. Opt.*, 40, pp. 3654-3658.

Baek, T.H., Kim, M.S., Morimoto, Y. and Fujigaki, M., 2002, "Separation of isochromatics and isoclinics from photoelastic fringes in a circular disk by phase measuring technique", *KSME International Journal*, Vol. 16, No. 2, pp. 175-181.

Chang, S.H. and Wu, H.H.P., 2011, "Improvement of digital photoelasticity based on camera response function", *Appl. Opt.*, 50, pp. 5263-5270.

Collett, E., 2005, "Field Guide to Polarization" (SPIE Vol. FG05), SPIE Publications, ISBN: 0819458686.

Corso, F.D., Bigoni, D. and Gei, M., 2008, "The stress concentration near a rigid line inclusion in a prestressed, elastic material. Part I: Full-field solution and asymptotics", *Journal of the Mechanics and Physics of Solids*, Vol. 56, Issue 3, pp. 815-838.

Estrada, J.C., Servin, M. and Quiroga, J.A., 2011, "Noise robust linear dynamic system for phase unwrapping and smoothing", *Opt. Express*, 19, pp. 5126-5133.

Fernandez, M.S.B., 2011, "Metrological study for the optimal selection of the photoelastic model in transmission photoelasticity", *Appl. Opt.*, 50, pp. 5721-5727.

Huang, M.J. and Sung P.C., 2010, "Regional phase unwrapping algorithm for photoelastic phase map", *Opt. Express*, 18, pp. 1419-1429.

Kihara, T., 2007, "Phase unwrapping method for three-dimensional stress analysis by scattered-light photoelasticity with unpolarized light. 2. Experiment", *Appl. Opt.*, 46, pp. 6469-6475.

Magalhaes P.A.A., Neto, P.S. and Barcellos, C.S., 2011, "Analysis of Shadow Moire Technique With Phase Shifting Using Generalisation of Carre Method", *Strain*, Vol. 47, Issue s1, pp. e555-e571, DOI: 10.1111/j.1475-1305.2009.00655.x.

Navarro, M.A., Estrada, J.C., Servin, M., Quiroga, J.A. and Vargas, J., 2012, "Fast two-dimensional simultaneous phase unwrapping and low-pass filtering", *Opt. Express*, 20, pp. 2556-2561.

Ng, T.W., 1997, "Derivation of retardation phase in computer-aided photoelasticity by using carrier fringe phase shifting", *Appl. Opt.*, 36, pp. 8259-8263.

Oh, J.T. and Kim, S.W., 2003, "Polarization-sensitive optical coherence tomography for photoelasticity testing of glass/epoxy composites", *Opt. Express*, 11, pp. 1669-1676.

Patterson, E.A. and Wang, Z.F., 1991, "Towards full field automated photoelastic analysis of complex components", *Strain*, Vol. 27, Issue 2, pp. 49-5.

Pinit, P. and Umezaki, E., 2007, "Digitally whole-field analysis of isoclinic parameter in photoelasticity by four-step color phase shifting technique", *Optics and Laser in Engineering*, Vol. 45, pp. 795-807.

Ramesh, K., 2000, "Digital photoelasticity: advanced techniques and applications", Springer-Verlag, Berlin, Germany.

Ramji, M. and Ramesh, K., 2008a, "Whole field evaluation of stress components in digital photoelasticity—issues, implementation and application", *Opt. Lasers Eng.*, 46(3), pp. 257-271.

Ramji, M. and Ramesh, K., 2008b, "Stress separation in digital photoelasticity, Part A—photoelastic data unwrapping and smoothing", *J. Aerosp. Sci. Technol.*, 60(1), pp. 5-15.

Ramji, M. and Ramesh, K., 2008c, "Stress separation in digital photoelasticity, Part B—whole field evaluation of stress components", *J. Aerosp. Sci. Technol.*, 60(1), pp. 16-25.

Ramji, M. and Prasath, R.G.R., 2011, "Sensitivity of isoclinic data using various phase shifting techniques in digital photoelasticity towards generalized error sources", *Optics and Lasers in Engineering*, Vol. 49, Issues 9-10, pp. 1153-1167.

Wijerathne, M.L.L., Oguni, K. and Hori, M., 2008, "Stress field tomography based on 3D photoelasticity", *Journal of the Mechanics and Physics of Solids*, Vol. 56, Issue 3, pp. 1065-1085.